

Communication

# Highly Active Nickel-Based Catalyst for Hydrogen Evolution in Anion Exchange Membrane Electrolysis

Alaa Y. Faid <sup>1,\*</sup> , Alejandro Oyarce Barnett <sup>2</sup>, Frode Seland <sup>1</sup>  and Svein Sunde <sup>1,\*</sup>

<sup>1</sup> Department of Materials Science and Engineering, Norwegian University of Science and Technology, NO-7491 Trondheim, Norway; frode.seland@ntnu.no

<sup>2</sup> SINTEF Industry, Sustainable Energy Technology Department, New Energy Solutions Group, Trondheim, Norway; AlejandroOyarce.Barnett@sintef.no

\* Correspondence: alaa.faid@ntnu.no (A.Y.F.); Svein.Sunde@ntnu.no (S.S.)

Received: 6 November 2018; Accepted: 29 November 2018; Published: 3 December 2018



**Abstract:** Anion exchange membrane (AEM) electrolysis is hampered by two main issues: stability and performance. Focusing on the latter, this work demonstrates a highly active NiMo cathode for hydrogen evolution in AEM electrolysis. We demonstrate an electrolyzer performance of 1 A cm<sup>-2</sup> at 1.9 V (total cell voltage) with a NiMo loading of 5 mg cm<sup>-2</sup> and an iridium black anode in 1 M KOH at 50 °C, that may be compared to 1.8 V for a similar cell with Pt at the cathode. The catalysts developed here will be significant in supporting the pursuit of cheap and environmentally friendly hydrogen fuel.

**Keywords:** Nickel; HER; anion exchange membrane; electrolysis

## 1. Introduction

Water electrolysis utilizing a solid polymer electrolyte membrane has been widely studied [1]. Compared to traditional alkaline water electrolysis that employs porous diaphragm separators with alkaline solution electrolytes, solid polymer electrolytes provide advantages such as lower gas crossover, improved efficiency, differential pressure operation, and improved operation dynamics [2]. Two types of solid polymer electrolytes are currently being pursued: proton exchange membranes (PEMs) and anion exchange membranes (AEMs) [3]. PEM water electrolysis (PEMWE) has matured considerably over the past decade, fulfilling many of the technical requirements for power-to-gas energy storage from renewables [4,5]. PEM electrolyzer technology still requires expensive catalysts based on noble metals, e.g., iridium and platinum, high cost perfluorinated polymers membranes such as Nafion [6].

AEM water electrolysis (AEMWE) has the potential to become a cheaper alternative to PEM water electrolysis systems, for example by allowing for the use of non-precious transition metal electrocatalysts [7]. Therefore, AEM water electrolysis aims to combine the low costs of alkaline electrolysis with the high power and flexibility of PEM electrolyzers [2]. However, the water splitting performance of AEM water electrolysis is currently much lower than that of PEMWE [8].

In general, the membrane electrode assembly (MEA) consists of a polymeric membrane with an anode and a cathode catalyst on each side of the membrane as shown in Figure 1. The catalyst can be coated on the membrane, thus forming a catalyst-coated membrane (CCM). Alternatively, catalyst ink can be coated on the porous substrate and compressed onto either side a polymer membrane forming catalyst-coated substrates (CCS) [9]. In AEM water electrolysis, hydrogen gas and hydroxide ions (OH<sup>-</sup>) produced from water reduction at the cathode while AEM exchanges (OH<sup>-</sup>) ions to the anode [10].



The overall reaction in Equation (1) requires catalytic activity, towards the oxygen evolution reaction (OER) at the anode and for the hydrogen evolution reaction (HER) at the cathode, to form the respective gases from the electrode surfaces [11]. The overall reaction requires a theoretical free energy electrolysis voltage or thermodynamic cell voltage of 1.23 V to get hydrogen and oxygen from water at 25 °C [12]. In practice, the cell voltage needed for efficient hydrogen generation must be higher than 1.23 V. Additional voltage is required to overcome over-voltages associated with electrode kinetics and the ohmic resistance of the electrolyte and electrolyzers components, among others [2,13].

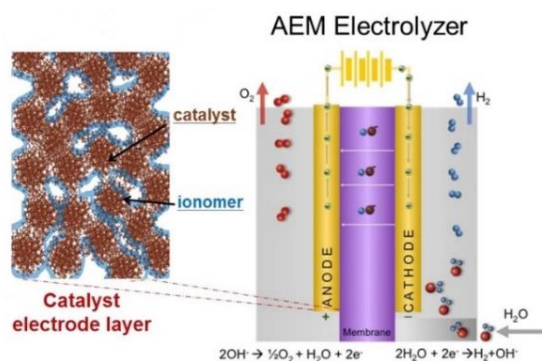


**Figure 1.** Catalyst electrode layer and membrane electrode assembly for anion exchange membrane (AEM) electrolyzer, where the catalyst is mixed with an ionomer, Reprinted from Artyushkova et al., License Number 4406040674790 [14].

Performance improvement through the development of new materials and optimization of the MEA fabrication process is of high importance. AEMs with high ionic conductivity and stability, as well as catalysts with improved activity and durability in alkaline conditions have been studied in various reports in recent years [3,15,16]. An et al. [17] developed a mathematical model to predict the performance of AEMWE. Their results showed that an activation polarization of the hydrogen and oxygen evolution reactions is responsible for the performance reduction (voltage to achieve specific current) in AEMWE. This points to the necessity of developing high-performance MEAs through electrocatalyst and membrane optimization [17,18].

Only a few studies address the influence of a non-precious metal catalyst cathode and hydroxide ion-conductivity in AEMWE devices. For example, Scott et al. [19] investigated the performance of AEMWEs using different cobalt-based oxides (2.5–3.0 mg cm<sup>-2</sup>) as the OER catalyst and Ni (2.0 mg cm<sup>-2</sup>) as the HER catalyst. At a 1.9 V cell voltage, the cell achieved current densities ranging from 65 mA cm<sup>-2</sup> (3.0 mg cm<sup>-2</sup> of Cu<sub>0.7</sub>Co<sub>2.3</sub>O<sub>4</sub>) to 175 mA cm<sup>-2</sup> (2.5 mg cm<sup>-2</sup> of Li-doped Co<sub>3</sub>O<sub>4</sub>). Comotti et al. [20] demonstrated the effect of HER catalyst (Ni/(CeO<sub>2</sub>-La<sub>2</sub>O<sub>3</sub>)/C) loading on AEMWE performance, the current density at 1.9 V increased from 160 to 470 mA cm<sup>-2</sup> as the loading varied from 0.6 to 7.4 mg cm<sup>-2</sup>. Xiao et al. investigated high catalyst loadings for both the HER (NiMo 40 mg cm<sup>-2</sup>) and OER (NiFe 40 mg cm<sup>-2</sup>) electrodes which resulted in AEMWE performance of 570 mA cm<sup>-2</sup> at 1.9 V [21]. This performance was comparable to that observed using PGM catalysts for the HER (Pt, 3.2 mg cm<sup>-2</sup>), and OER (IrO<sub>2</sub>, 2.9 mg cm<sup>-2</sup>) electrodes, respectively [21].

In this paper, we show that our synthesized NiMo catalyst offers a cathode performance comparable to Pt nanoparticle catalyst in AEMWE. We also include a description of the influence of the KOH concentration on the performance of NiMo HER catalysts in a real AEMWE environment.

## 2. Results and Discussion

The NiMo catalyst was prepared by reducing an aqueous solution containing the Ni and Mo metal precursors in presence of sodium borohydride. SEM images of the amorphous catalysts are shown in Figure 2. The catalyst exhibited nanosheet-like structures. A similar nanosheet morphology has also been obtained for NiFe prepared by reduction of precursors with NaBH<sub>4</sub> [22]. These nanosheets

are loosely stacked and form sponge-like structures, leading to high specific surface areas. Here we used X-ray diffraction (XRD) to investigate crystal structure and phases present in the NiMo catalyst. The XRD pattern for NiMo in Figure 2 shows two broad peaks consistent with an amorphous catalyst powder, a very small crystallite size, or both. The XRD pattern does not display any sharp peaks that may be related to an extended periodicity of the lattice [23].

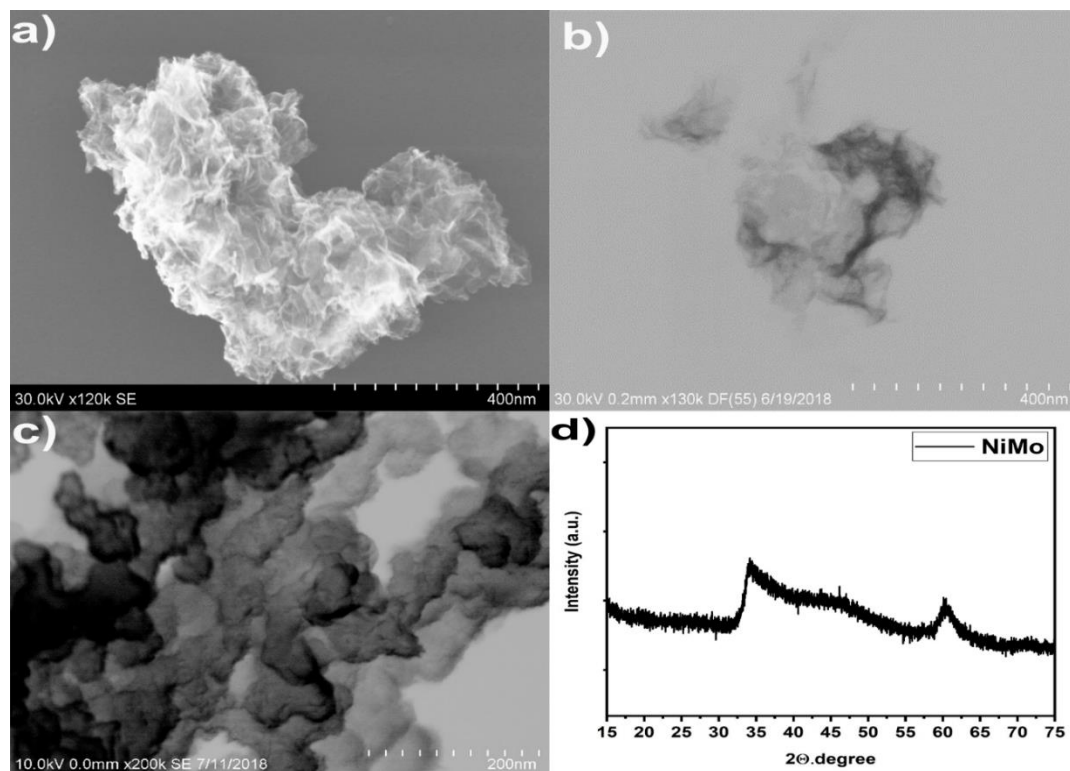


**Figure 2.** (a) SEM image of Ni<sub>0.9</sub>Mo<sub>0.1</sub> nanosheets, (b) Inverted dark field scanning transmission electron microscopy (STEM) Ni<sub>0.9</sub>Mo<sub>0.1</sub> nanosheets (c) Ni<sub>0.9</sub>Mo<sub>0.1</sub> supported in Vulcan XC72 prepared by chemical reduction, (d) X-ray diffraction pattern of Ni<sub>0.9</sub>Mo<sub>0.1</sub> nanosheets.

Raman spectroscopy was employed to evaluate the vibrational modes of the NiMo catalyst. The Raman spectra reproduced in Figure 3 contain peaks corresponding to the one-phonon (1P) and two-photon (2P) NiO Raman modes at 570 and 1090 cm<sup>-1</sup>, respectively [24]. Although Raman phonon modes (1P and 2P) shown in Figure 3 are identical to those in the single-crystal, the 1P mode may also be associated with bulk defects or surfaces [24].

The X-ray photoelectron spectroscopy (XPS) spectrum in Figure 3 of the NiMo nanosheets displays three peaks at 230.6, 402, and 410 eV, related to Mo3d, Mo3p<sub>3/2</sub>, and Mo3p<sub>1/2</sub> levels of molybdenum, respectively. These peaks can be assigned to presence of the Mo<sup>4+</sup> (4d<sup>2</sup>) states of molybdenum oxide [25]. The high resolution peaks of Mo3d<sub>5/2</sub> (230.1 eV) and Mo3d<sub>3/2</sub> (233.3 eV) are related to the Mo<sup>4+</sup> oxidation state (MoO<sub>2</sub>) on the surface [26]. In addition, the NiMo XPS spectra of the NiMo nanosheets contain peaks corresponding to the Ni2p<sub>3/2</sub> and Ni2p<sub>1/2</sub> levels with binding energies 854 and 873 eV, respectively, which suggests the presence of Ni in an oxidized state [27]. Auger peaks of Ni appears in the binding energy range from 600 to 800 eV. A peak with a binding energy of 187.0 eV corresponds to the of the B<sub>1s</sub> level of elemental boron [28,29] The XPS data are thus consistent with the presence of surface oxide states of Ni and Mo in the NiMo nanosheets.

The electrocatalytic performance of the NiMo and Pt/C catalysts were evaluated in a three-electrode system in N<sub>2</sub>-saturated 1 M KOH electrolyte with a rotating disk electrode (RDE). Figure 4 shows the current recorded during linear sweep voltammetry (LSV) for NiMo catalysts with a Mo content with 3%, 5%, and 10%, respectively. As can be seen from Figure 4a, the current density

normalized to the geometric surface area, and thus the catalytic activity is dependent on composition.  $\text{Ni}_{0.9}\text{Mo}_{0.1}$  exhibits the highest electrochemical activity. It is worth noting that bare glassy carbon and Vulcan XC/72 support have almost negligible hydrogen evolution activity. The evaluation of the ECSA of NiMo presented here is based on the double layer capacitance procedure [30,31]. For Pt/C, the ECSA was calculated from the area under  $\text{H}_{\text{upd}}$  peak [32]. As for the mass activity, we kept the catalyst loading at the electrode at  $0.25 \text{ mg/cm}^2$  and the glassy carbon electrode geometric surface area of  $S_{(\text{geo})} = 0.196 \text{ cm}^2$ . Mass activity ( $\text{A/g}$ ) was calculated from the actual catalyst loading (in  $\text{mg/cm}^2$ ) and current density  $j$  ( $\text{mA/cm}^2$ ) at a given overpotential [33].

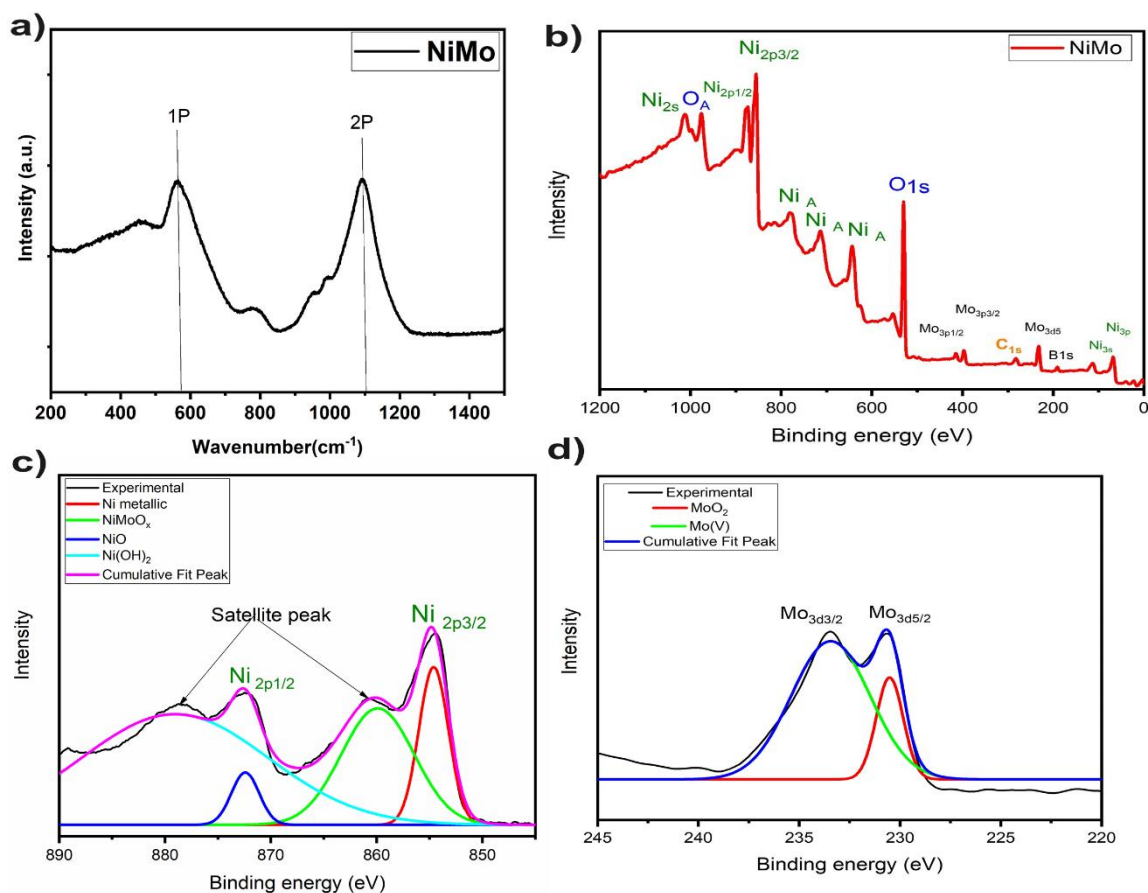


**Figure 3.** (a) Raman spectrum of  $\text{Ni}_{0.9}\text{Mo}_{0.1}$  nanosheets, (b) X-ray photoelectron spectroscopy (XPS) spectrum of  $\text{Ni}_{0.9}\text{Mo}_{0.1}$  nanosheets, (c) XPS peak fitting of Nickel peaks (d) XPS peak fitting of Mo peaks.

To reach the benchmark activity of  $-10 \text{ mA/cm}^2$  Pt required an overpotential of  $-105 \text{ mV}$ , while  $\text{Ni}_{0.9}\text{Mo}_{0.1}$  required  $-185 \text{ mV}$ . The Tafel slope for NiMo is about  $-120 \text{ mV}$ , which is larger than that for Pt/C  $-70 \text{ mV/dec}$ . The HER kinetics of the NiMo catalyst thus appears to be consistent with electrochemical adsorption as the rate-determining step for the HER. The Tafel slope is therefore consistent with both the Volmer–Heyrovsky and Volmer Tafel mechanisms [34].

Electrochemical investigation of NiMo and Pt in half-cell measurements were done with the same mass loading and the weight ratio ( $\text{Pt/NiMo} = 1:1$ ). The trend in Figure 4, shows that Pt has higher HER activity than NiMo. Based on measurements in the electrochemical cell, the mass loading of Ni should be five times higher than that of Pt to attain comparable activity. Based on cost analysis, owing to the price difference between Ni (10 cents ( $\text{¢}$ ) per gram), Mo (10 cents ( $\text{¢}$ ) per gram), and Pt (30 USD per gm), with a NiMo: Pt weight ratio of 5:1 the HER catalyst cost would be reduced at least 60 times [35]. Such a cost reduction cost is highly beneficial for applications in industry and energy systems.

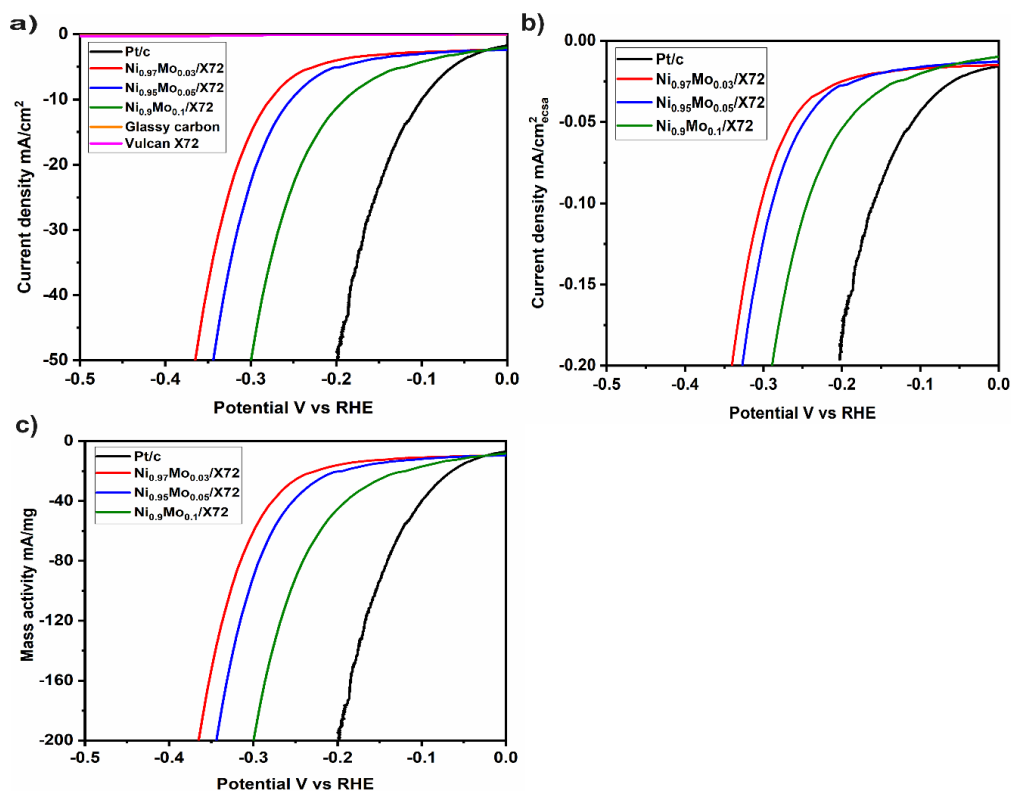


**Figure 4.** Linear sweep voltammetry (LSV) of NiMo with different Mo composition and Pt/C normalized to (a) geometric surface area and (b) electrochemical surface area and (c) mass loading.

Electrochemical impedance spectroscopy (EIS) was carried out for investigation of the electrode-electrolyte interface kinetics. Figure 5a shows the Nyquist plots of Ni<sub>0.9</sub>Mo<sub>0.1</sub> and Pt/C at different applied potentials (−150 and −100 mV vs. RHE) in 1 M KOH. Pt and Ni<sub>0.9</sub>Mo<sub>0.1</sub> have similar high-frequency resistances. For Pt and NiMo at higher applied potential, the radius of the semicircle decreases, signifying a lower charge transfer resistance ( $R_{ct}$ ) as expected if the current depends exponentially on potential [36,37].

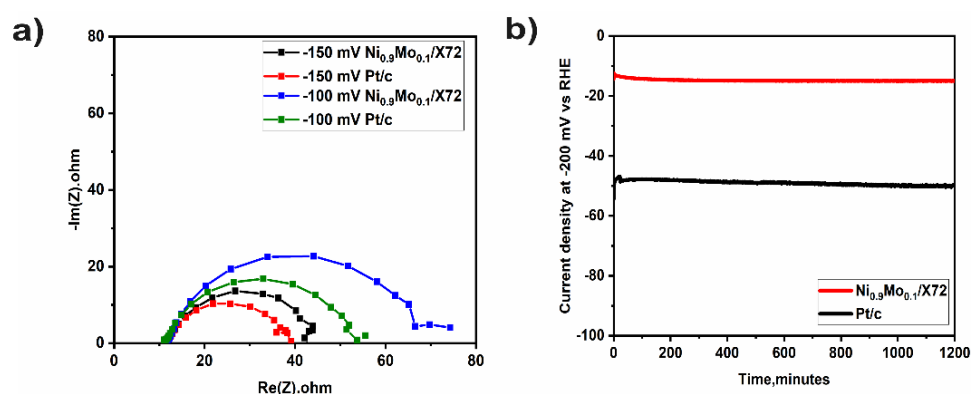


**Figure 5.** (a) Nyquist plot of Ni<sub>0.9</sub>Mo<sub>0.1</sub> and Pt/C in 1 M KOH at −150 and 150 mV vs. RHE (b) Chronoamperometry of Ni<sub>0.9</sub>Mo<sub>0.1</sub> and Pt/C for 24 h in 1 M KOH.

Chronoamperometric measurements were performed by applying constant potentials of −200 mV for 1200 min. From Figure 5b, Ni<sub>0.9</sub>Mo<sub>0.1</sub> in 1 M KOH displays short-term stability which is similar to that of Pt/C at this applied overpotential. These results thus indicate that the Ni<sub>0.9</sub>Mo<sub>0.1</sub> electrocatalysts have good short-term stability [38].

Based on structural and the evaluation of catalyst activity in the electrochemical cell, (Ni<sub>0.9</sub>Mo<sub>0.1</sub>) have the best HER activity and durability among the NiMo catalysts and have therefore been chosen to represent NiMo in AEM water electrolysis cell.

In AEMWE cell Pt/C or NiMo supported on Vulcan x72 carbon (NiMo/X72) were used as cathode catalysts while Ir black served as the anode catalyst. Reinforced Fumatech membranes, Fumapem FAA-3-PE-30 and 10 wt. % Fumion FAA-3-solute-10 ionomer in NMP were utilized in the MEA preparation. The MEAs (shown in Figure S1 in the ESI<sup>†</sup>) were assembled in a modified Baltic cell hardware between two commercially available porous Ti transport layers for water electrolysis (Beakaert).

The morphology of the catalyst layer is best described as catalyst particles covered with ionomer and electrolyte as illustrated in Figure 1. Compositional uniformity along catalyst layers was confirmed by energy dispersive X-ray (EDX) mapping as illustrated in Figure S2 in the ESI<sup>†</sup>; the elemental mapping shows a uniform distribution of Ni, Mo, O, and carbon. The ink is sprayed in the whole membrane area, Nickel percentage in the catalyst is 90% while Mo is only 10%, that is why by EDX we can see Nickel is more pronounced in Figure S2. The cross-sectional interface view of the cathode MEA demonstrated in Figure S2 (ESI<sup>†</sup>) confirmed the uniform dispersion of the catalyst along the MEA layer and its firm adherence to the membrane. SEM images (Figure S3, ESI<sup>†</sup>) show that the distribution of catalyst is also uniform across the surface of the AEM; the SEM images revealed no voids or cracks in the catalyst layer.

Electrochemical impedance spectroscopy (EIS) during in-situ full cell testing was conducted to provide information about the uncompensated resistance and then to separate the ohmic resistance from other contributions to the voltage of the AEMWE cells. Figure 6 shows the impedance-plane plot at 0.4 A cm<sup>-2</sup> for the cells with NiMo/X72 cathodes (Figure 6a) and Pt/C cathodes (Figure 6b) for both 0.1 and 1.0 M KOH. The impedance-plane plots appear to consist of two partly overlapping and depressed semicircles. (A high-frequency tail extending towards positive imaginary parts is considered to be due to the electronics and the experimental setup and is not considered further in this work). The low-frequency arcs are of a similar size for the two catalysts, whereas the high-frequency arc has a significantly larger radius for the NiMo catalyst than for Pt.

The total ohmic resistance of the 25 cm<sup>2</sup> cell was determined from the high-frequency resistance (HFR), i.e., from the intercept with the real (Re) axes of the impedance-plane plot [39]. For 1 M KOH, NiMo/X72 cell has an HFR of approximately 0.150 Ω cm<sup>2</sup>, which is lower compared to the Pt/C based AEMWE cell (0.190 Ω cm<sup>2</sup>). This shows that despite having higher NiMo loadings resulting in thicker catalyst layers, the NiMo/X72 cell still shows excellent cell conductivity. However, a considerable increase in the HFR was observed when changing the KOH concentration to 0.1 M KOH; 0.310 Ω cm<sup>2</sup> for NiMo/X72 and 0.290 Ω cm<sup>2</sup> for Pt/C. This HFR increase at the lower KOH concentration may indicate insufficient ionic conductivity of the membrane [26]. The conductivity of the membrane is directly proportional to KOH concentration until reaches 5 M KOH. Beyond this concentration, the membrane conductivity tends to decrease as KOH concentration increases [40]. Stefania et al. [41] found similar behaviour for Pt/C. The HFR increases when the catalyst loading decreases, which might be associated with constriction resistances [42]. However, it is difficult to unequivocally relate the change in the HFR with KOH concentration for the two catalysts to constriction resistances. Newman et al. [43] showed that electrochemical reactions are nonuniformly distributed within the electrode. The distribution will be dependent on the ohmic resistance in pores as well as the charge transfer kinetics. For slow kinetics, the reaction is forced to be more uniformly distributed than for fast kinetics. The former case would correspond to the NiMo and the latter to Pt/C. The contribution to the changes in impedance with KOH concentration from the pore resistance would thus be expected to be more significant the more evenly the reaction is distributed. While this may contribute to the larger changes in the radius of the arcs in Figure 6 for the NiMo sample than for Pt/C, an interpretation of the changes of the high-frequency intercepts with concentration will require investigation going beyond the scope here.

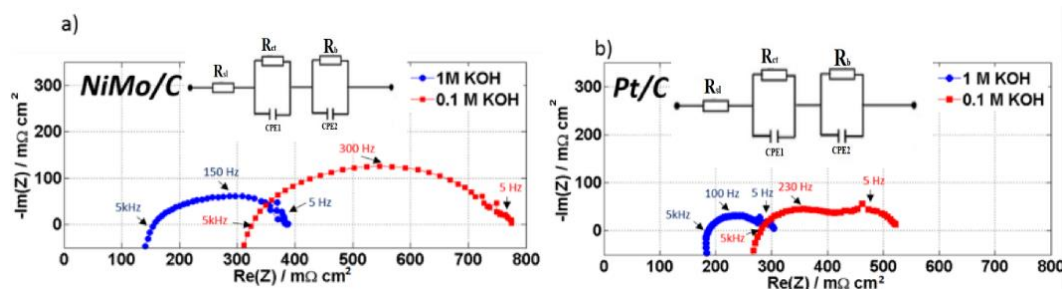


**Figure 6.** Electrochemical impedance is taken at 0.4 A in both 1 M and 0.1 M KOH at 50 °C. (a) A 5 mg cm<sup>-2</sup> NiMo loading compared to (b) a 1 mg cm<sup>-2</sup> Pt. Cell active area: 25 cm<sup>-2</sup>. Both catalyst coated membranes (CCMs) using 3 mg cm<sup>-2</sup> Ir-black. The impedance data represented by symbols and the fitted impedance data represented by a solid line.

We emphasize that apart from the cathode catalyst layers, the two cells were constructed using the same components, i.e., using the same type of bipolar plates, porous transport layers, anode catalyst layers, and membranes. Therefore, the differences in the EIS of the different cells are attributed to the cathode catalyst layer only.

The low-frequency arc at around 5 Hz (Figure 6) being of similar magnitude in the two cases, may be attributed to mass transport [39,44] or the anode [44]. The much larger high-frequency arc, on the other hand, indicates significant differences in the kinetic contributions to the cell voltage from the NiMo/X72 and Pt/C cathodes. For analysis, we converted the recorded impedance data to Tafel impedance [33], i.e., the impedance multiplied with the steady-state current density at which it was obtained. For a kinetically limited process, the Tafel slope for the reaction can be found from the Tafel impedance as the diameter of the impedance arc [45,46]. Assuming that the entire impedance consists of kinetic contributions in Figure 6, we thus estimate the Tafel slope in 1 M KOH to be 50 mV for Pt and 95 mV for NiMo (Table S1 ESI†) at 0.4 A cm<sup>-2</sup>. Even if the low-frequency arc may be due to other processes than that can be ascribed to the HER at the cathode, Figure 6, and (Figures S4 and S5, ESI†) indicates that the Tafel slope for the NiMo cell is twice that of Pt under the same process conditions. Thus, the reaction mechanism is different at NiMo cell than at Pt cell.

In Figure 6, we show the equivalent circuit that used to fit the impedance data. The equivalent circuit on Figure 6 is used to fit the impedance data taken at 0.4 A in both 1 M and 0.1 M KOH at 50 °C. Ni<sub>0.9</sub>Mo<sub>0.1</sub> and Pt/C cells. The fitted electrical circuit is comprised of two parallel circuits containing a resistor and a constant-phase element (CPE) each in series with a resistor. The latter, R<sub>e1</sub>, is attributed to the ohmic resistance of the cell (current collectors and membrane). We take the balance of the circuit to represent charge transfer, adsorption of intermediates and double layer capacitance in a porous electrode layer [39,41]. A detailed interpretation is, however, beyond the scope here.

Figure 7 shows the potentiostatic polarisation curves of both iR-corrected and uncorrected voltages for the AEMWE at different KOH concentration, both for cells with cathode MEAs containing NiMo/X72 and Pt/C (standard deviation is <1(10<sup>-3</sup>) for three measurements). For the polarisation curves that were corrected for ohmic resistance we used the following equation:

$$V_{iR} = V - (iRA) \quad (2)$$

where V<sub>iR</sub> is the potential corrected for resistance; i is the current density in units of A cm<sup>-2</sup>; A is the geometric area of the AEMWEs in cm<sup>2</sup>, and R is the area specific resistance measured by impedance and in the units of Ω cm<sup>2</sup>. The current-voltage characteristics for the NiMo cells appear to be more curved than those for the Pt cells, both for the iR-corrected and uncorrected data. Also, the slopes of the iV-curves are larger for the cells with NiMo than those with Pt, in line with Tafel slopes from the impedance measurements.

Despite higher slightly onset potentials for NiMo/X72 compared to Pt/C, the NiMo cell displays an excellent performance (Figure 7), being comparable to that of the cell with the Pt cathode,

achieving  $1 \text{ A cm}^{-2}$  at  $1.9 \text{ V}$  in  $1 \text{ M KOH}$ . The corresponding performance for the Pt cell is  $1 \text{ A cm}^{-2}$  at  $1.8 \text{ V}$  in  $1 \text{ M KOH}$ .

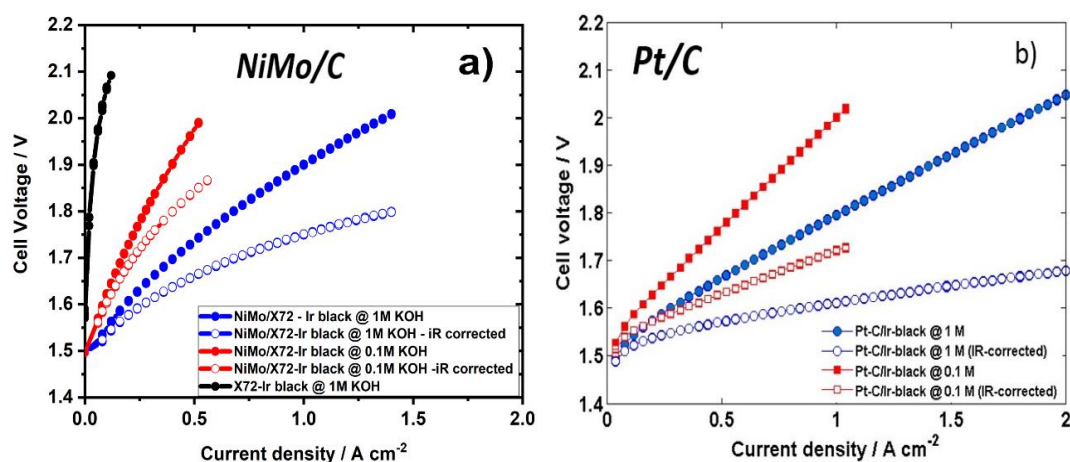


**Figure 7.** Polarization curves in both  $1 \text{ M}$  and  $0.1 \text{ M KOH}$  at  $50 \text{ }^\circ\text{C}$ . (a) A  $5 \text{ mg cm}^{-2}$  NiMo loading compared to (b) a  $1 \text{ mg cm}^{-2}$  Pt. Cell active area:  $25 \text{ cm}^{-2}$ . Both CCMs using  $3 \text{ mg cm}^{-2}$  Ir-black.

In  $0.1 \text{ M KOH}$ , the difference was larger, the NiMo cell yielding  $0.5 \text{ A cm}^{-2}$  at  $2 \text{ V}$  and the Pt cell the same current at  $1.65 \text{ V}$ . On the other hand, low KOH concentrations ( $<1 \text{ M}$ ) does have a more adverse effect for the NiMo cell than for the Pt cell. The activity decrease in  $0.1 \text{ M KOH}$  could be related to membrane conductivity which decreases at lower KOH concentrations [40]. The different reaction mechanisms implied by the differences in Tafel impedance also suggest that the mechanisms and the reaction orders are different at the two cathodes. A contribution to the pH dependence on the overall cell performance from the cathode should therefore also be expected, as is rather clearly demonstrated in Figure 7.

The excellent performance of  $1 \text{ A cm}^{-2}$  at  $1.75 \text{ V}$  (iR-corrected) in  $1 \text{ M KOH}$  obtained for the NiMo/X72 hydrogen catalyst outperforms all of those summarized in Table S2 ESI†. Nowadays, commercial alkaline electrolyzers reach current densities up to  $0.45 \text{ A cm}^{-2}$  at a cell voltage of  $1.7\text{--}2.1 \text{ V}$ , corresponding to a theoretical hydrogen generation rate of  $1.9 \text{ Nm}^3$  per  $\text{m}^3$  of the cell area [18]. Therefore NiMo/X72 catalyst potentially allows for low loading transition metal loading in AEMWE operation on a commercial scale [18,47].

### 3. Materials and Methods

#### 3.1. Chemicals and Materials

NiMo/X72 prepared in our lab, Commercial Pt/C (Alfa Aesar 60% on carbon support, Massachusetts, USA) and Ir black (Alfa Aesar 99.8% S.A  $> 20 \text{ m}^2/\text{g}$ ), Fumatech ionomer: Fumion FAA-3-SOLUT-10 anion exchange polymer solution N-methyl-2-pyrrolidone (NMP) solvent solution, concentration 10 wt. % purchased from Fumatech BWT group, Germany. Fumapem FAA 3-PE membrane: Anion exchange Membrane  $20\text{--}30 \text{ }\mu\text{m}$ ) purchased from Fumatech BWT group, Germany. Sigma Aldrich (Sigma-Aldrich Chemie GmbH, Munich, Germany) supplied reagent grade Isopropanol (IPA). All chemicals were used as received and deionized (D.I) water used was of  $18.2 \text{ M}\Omega\cdot\text{cm}$  resistivity.

**NiMo Catalyst Synthesis:** NiMo nanosheet prepared by a simple chemical reduction at  $20 \pm 2 \text{ }^\circ\text{C}$  as reported by many groups for other transition metals [48,49]. In this process we reduced  $200 \text{ mL}$  of aqueous mixture of ammonium molybdate tetrahydrate  $(\text{NH}_4)_6\text{Mo}_7\text{O}_{24}\cdot 4\text{H}_2\text{O}$  and nickel nitrate hexahydrate  $\text{Ni}(\text{NO}_3)_2\cdot 6\text{H}_2\text{O}$  with molar concentration of Ni:Mo (0.9:0.1) in the presence of sodium borohydride ( $\text{NaBH}_4$ ) to produce  $\text{Ni}_{0.9}\text{Mo}_{0.1}$  supported on Vulcan carbon XC/72 (60 wt. %). Sodium borohydride concentration was three times that of the metal precursor to ensure full reduction

and compensate for the hydrogen gas evolution. The final solution was centrifuged and dried under vacuum at room temperature.

### 3.2. Catalyst Characterization

#### 3.2.1. Structural Characterization

The morphology of the NiMo nanosheets was studied Using scanning electron microscopy (SEM, Carl Zeiss supra 55, Oberkochen, Germany). NiMo nanosheets were investigated using Hitachi s-5500 FESEM (Krefeld, Germany), using Scanning transmission electron microscopy (STEM) mode, NiMo dissolved in ethanol and the solution deposited on Formvar/Carbon 300 mesh, Copper grid hole size: 63  $\mu\text{m}$ . Structural and crystalline characteristics of the nanosheets were investigated using a Bruker D8 A25 DaVinci X-ray Diffractometer with  $\text{CuK}\alpha$  radiation (Billerica, Massachusetts, USA). The average wavelength of the radiation was 1.5425  $\text{\AA}$ . Raman spectroscopy was carried out with a Renishaw InVia-Reflex Spectrometer using VIS excitation at 532 nm (100 mW) with spectral resolution  $<1 \text{ cm}^{-1}$ . Surface electronic states and composition of NiMo nanosheets were carried out by X-ray photoelectron spectroscopy (XPS). XPS spectra were collected within an Axis Ultra DLD instrument (Kratos Analytical, Manchester, UK) equipped with a monochromatic Al X-ray source.

#### 3.2.2. Preparation of the Electrode for RDE Measurement

The catalyst ink was prepared by homogenization of 5 mg of catalyst material in a solution of (0.5 mL D.I water, 0.44 mL Isopropanol + 60  $\mu\text{L}$  Nafion 117 solution). The ink sonicated in an ultrasonication bath for 30 min. An aliquot of homogenized catalyst ink was deposited onto a glassy carbon electrode. The shaft was rotated at 100 rpm (mass loading was kept at  $0.25 \text{ mg/cm}^2$ ). The ink was subsequently dried in air at room temperature by maintaining the rotator speed at 700 rpm for 15 min.

#### 3.2.3. Electrochemical Characterization

The electrochemical measurements were carried out using a multi-channel electrochemical analyzer (Ivium-n-Stat). A rotating disk electrode (RDE) (PINE Research Instrumentation, (Durham, NC, USA), modified as described before, was used as a working electrode. Platinum foil served as a counter-electrode. The Hg/HgO (Pine Research) was used as a reference electrode. Nitrogen-saturated 1 M KOH solution was used as an electrolyte. It was freshly prepared before each set of experiments. LSV curves were collected in a potential range of  $-0.4$  to  $-1.9 \text{ V}$  vs. Hg/HgO using a scan rate of  $5 \text{ mV/s}$  at 1600 rpm rotation speed. All electrochemical experiments were done at a temperature of  $22 \pm 2 \text{ }^\circ\text{C}$ . All resulting data were corrected for IR loss due to the solution resistance. The equation corrected the compensated potential:

$$E_{\text{compensated}} = E_{\text{measured}} - iR$$

where  $E_{\text{compensated}}$  and  $E_{\text{measured}}$  denote as the compensated and measured potentials, respectively.

Short-term durability and stability test was carried out using chronoamperometry for 20 h at  $-200 \text{ mV}$  constant cathodic overpotential. Electrochemical impedance spectroscopy (EIS) measurements at selected potentials were carried out in range of 0.1 Hz to 100 kHz in 1M KOH. All potentials measured were calibrated to RHE using:

$$E_{\text{RHE}} = E_{\text{Hg/HgO}} + 0.098 \text{ V} + (0.059 \text{ V pH}).$$

### 3.3. MEA Preparation

Ink preparation: the mixing procedure includes: (1) add required amount of water (4.8 gm) and ionomer (1.92 g (gm)) to catalyst powder then sonicate with ice for 15 min. (2) add IPA (4.8 gm).

(3) sonicate for 10 min with ice. (4) Mix with an ultrasonic probe (the ultrasonic probe is Branson Digital Sonifier model 102c) for 5 min with ice, amplitude = 40%. (Sonication is to ensure a good mixture of ink and to keep it un-agglomerated, and it is done at  $5 \pm 2$  °C, the uniformity of ink composition is essential to ensure reproducible results). For these experiments, we keep NiMo/X72 loading  $5 \text{ mg/cm}^2$  and Ir loading  $3 \text{ mg/cm}^2$ .

**Spraying MEA:** The  $25 \text{ cm}^2$  AEM catalyst coated membranes (CCMs) were prepared by spraying (airbrush) catalyst directly on to membranes mounted to a temperature controlled hot plate at  $60$  °C, a slower rate of spraying resulted in better CCM. The MEAs were fabricated using airbrush spraying. The fumatech membrane was assembled in a plastic holder that functions as a mask as well to leave only the active area open to deposition. A commercial Coltech airbrush spraying ( $0.35 \text{ mm}$  nozzle) was used during the deposition. There are 10 min waiting between cathode and anode spraying.

The MEAs were conditioned and exchanged to the OH form in-situ. The water electrolyzer setup consisted of a 5 L Teflon tank with heaters and a peristaltic pump, which was used to pump hot KOH ( $50$  °C) through the AEMWE cell. The cells were always filled with the KOH solution during operation and were not exposed to ambient air. This eliminates some of the drawbacks associated with AEM in fuel cells, e.g., membrane degradation due to dry conditions and precipitation of carbonates.

### 3.4. Cell Testing

**For single cell tests:** The MEAs were assembled in a modified Baltic cell hardware between two commercially available Ti porous transport layer for water electrolysis (Beakaert). The MEA was conditioned and exchanged to the OH form in-situ. The setup consists of 5 L Teflon tank with heaters and a peristaltic pump to pump hot KOH through the AEMWE cell. The cell was operated at  $50$  °C and atmospheric pressure, KOH was fed in anode and cathode sides. During cell testing, MEA with carbon only as a cathode was used to evaluate the activity of the cell without NiMo catalyst.

For electrochemical analyses, a high-current potentiostat (HCP-803, Bio-Logic, Seyssinet-Pariset, France) was used to control cell voltage and measure impedance. The current density was measured for repeated voltage cycles from 1.5 to 2 V. Electrochemical impedance spectroscopy (EIS) was employed to determine the cell performance-affecting resistances for different operating and electrode fabrication conditions, with the corresponding analyses performed at different current densities such as 0.1, 0.4, and  $0.8 \text{ A/cm}^2$  in the AC frequency range of 50 kHz–200 mHz.

### 3.5. SEM and EDX Mapping

The catalyst layers on the MEA and the cross-sectional view were examined by high-resolution scanning electron microscopy (SEM); Zeiss supra 55 was used. Samples were prepared by cutting  $1.0 \text{ mm}$  wide strips from the different MEA and fixed on aluminum holders before analysis.

## 4. Conclusions

In summary, we have demonstrated that the use of amorphous NiMo catalyst supported on carbon as cathode leads to AEM water electrolysis cell achieving  $1 \text{ A cm}^{-2}$  at  $1.75 \text{ V}$  (iR-corrected) in  $1 \text{ M KOH}$  supporting electrolyte. This shows that the performance of AEM water electrolysis may be achieved at levels (especially on a cost vs. current basis) of significant commercial interest.

**Supplementary Materials:** The following are available online at <http://www.mdpi.com/2073-4344/8/12/614/s1>, Figure S1: photograph of an individual MEA, Figure S2: (a) SEM image of MEA cross-section, (b) EDX mapping of MEA prepared by airbrush spraying, and individual elemental mapping for Ni, Mo, O, and C, respectively, Figure S3: (a) SEM image of NiMo/x72 cathode surface in MEA, (b) SEM image of Ir anode surface in MEA prepared by airbrush spraying, Figure S4: Tafel analysis of (a) NiMo/X72 cell and (b) Pt/C cell in 1 and 0.1 M KOH, Figure S5: Tafel impedance analysis of (a) and (b) NiMo/X72 cell in 0.1 M and 1 M KOH, respectively, (c) and (d) Pt/C cell in 0.1 and 1 M KOH, respectively, Table S1: Tafel impedance of NiMo/X72 cell and Pt/C cell in 0.1 and 1M KOH at different current density, Table S2: Review of AEM water electrolysis performance and development.

**Author Contributions:** Synthesis, electrochemical measurements, SEM, STEM, XRD, Raman, XPS data analysis, writing and editing, A.Y.F. In-situ electrolysis testing, Funding acquisition, supervision, review and editing, A.O.B.; Supervision, funding acquisition, review, and editing, F.S.; Funding acquisition, supervision, review, and editing, S.S.

**Funding:** This research was funded by The Norwegian Research Council through the ENERGIX program contract number 268019, and The APC was funded by NTNU Publishing Fund.

**Acknowledgments:** Financially support from the Research Council of Norway, ENERGIX, HAPEEL, project number 90218402, is greatly acknowledged. The Research Council of Norway is acknowledged for the support to the Norwegian Micro- and Nano-Fabrication Facility, NorFab, project number 245963/F50.

**Conflicts of Interest:** There are no conflicts to declare.

## References

1. Vincent, I.; Kruger, A.; Bessarabov, D. Development of efficient membrane electrode assembly for low cost hydrogen production by anion exchange membrane electrolysis. *Int. J. Hydrogen Energy* **2017**, *42*, 10752–10761. [[CrossRef](#)]
2. Leng, Y.; Chen, G.; Mendoza, A.J.; Tighe, T.B.; Michael, A.; Hickner, M.A.; Wang, C.-Y. Solid-state water electrolysis with an alkaline membrane. *J. Am. Chem. Soc.* **2012**, *134*, 9054–9057. [[CrossRef](#)]
3. Varcoe, J.R.; Atanassov, P.; Dekel, D.R.; Herring, A.M.; Hickner, M.A.; Kohl, P.A.; Kucernak, A.R.; Mustain, W.E.; Kitty Nijmeijer, K. Anion-exchange membranes in electrochemical energy systems. *Energy Environ. Sci.* **2014**, *7*, 3135–3191. [[CrossRef](#)]
4. Sapountzi, F.M.; Gracia, J.M.; (Kees-Jan) Weststrate, C.J.; Fredriksson, H.O.A.; (Hans) Niemantsverdriet, J.W. Electrocatalysts for the generation of hydrogen, oxygen and synthesis gas. *Prog. Energy Combust. Sci.* **2017**, *58*, 1–35. [[CrossRef](#)]
5. Grond, L.; Schulze, P.; Holstein, J. Systems Analyses Power to Gas. *DNV Kema* **2013**, GCS 13.R.2, 1–70.
6. Kuckshinrichs, W.; Ketelaer, T.; Koj, J.C. Economic Analysis of Improved Alkaline Water Electrolysis. *Front. Energy Res.* **2017**, *5*. [[CrossRef](#)]
7. Gong, M.; Wang, D.Y.; Chen, C.C.; Hwang, B.J.; Dai, H. A mini review on nickel-based electrocatalysts for alkaline hydrogen evolution reaction. *Nano Res.* **2016**, *9*, 28–46. [[CrossRef](#)]
8. Kyung, M.; Park, H.-Y.; Choe, S.; Yoo, S.J.; Kim, J.Y.; Kim, H.-J.; Henkensmeier, D.; Lee, S.Y.; Sung, Y.-E.; Park, H.S.; Jang, J.H. Factors in electrode fabrication for performance enhancement of anion exchange membrane water electrolysis. *J. Power Sources* **2017**, *347*, 283–290.
9. Phillips, R.; Dunnill, C.W. Zero gap alkaline electrolysis cell design for renewable energy storage as hydrogen gas. *RSC Adv.* **2016**, *6*, 100643–100651. [[CrossRef](#)]
10. Xiang, C.; Papadantonakis, K.M.; Lewis, N.S. Principles and implementations of electrolysis systems for water splitting. *Mater. Horiz.* **2016**, *3*, 169–173. [[CrossRef](#)]
11. Eftekhari, A. Electrocatalysts for hydrogen evolution reaction. *Int. J. Hydrogen Energy* **2017**, *42*, 11053–11077. [[CrossRef](#)]
12. Li, X.; Hao, X.; Abudula, A.; Guan, G. Nanostructured catalysts for electrochemical water splitting: Current state and prospects. *J. Mater. Chem. A* **2016**, *4*, 11973–12000. [[CrossRef](#)]
13. Bladergroen, B.; Su, H.; Pasupathi, S.; Linkov, V. Overview of Membrane Electrode Assembly Preparation Methods for Solid Polymer Electrolyte Electrolyzer. In *Electrolysis*; IntechOpen: London, UK, 2012.
14. Artyushkova, K.; Serov, A.; Doan, H.; Danilovic, N.; Capuano, C.B.; Sakamoto, T.; Kishi, H.; Yamaguchi, S.; Mukerjee, S.; Atanassov, P. Application of X-ray photoelectron spectroscopy to studies of electrodes in fuel cells and electrolyzers. *J. Electron Spectros. Relat. Phenom.* **2017**. [[CrossRef](#)]
15. Kyung, M.; Park, H.-Y.; Lee, H.J.; Kim, H.-J.; Lim, A.; Sung, D.H.; Jin, J.Y.; So, Y.K.; Lee, Y.; Park, H.S.; Jang, J.H. Alkaline anion exchange membrane water electrolysis: Effects of electrolyte feed method and electrode binder content. *J. Power Sources* **2018**, *382*, 22–29.
16. Sassin, M.B.; Garsany, Y.; Gould, B.D.; Swider-Lyons, K.E. Fabrication Method for Laboratory-Scale High-Performance Membrane Electrode Assemblies for Fuel Cells. *Anal. Chem.* **2017**, *89*, 511–518. [[CrossRef](#)] [[PubMed](#)]
17. An, L.; Zhao, T.S.; Chai, Z.H.; Tan, P.; Zeng, L. Mathematical modeling of an anion-exchange membrane water electrolyzer for hydrogen production. *Int. J. Hydrogen Energy* **2014**, *39*, 19869–19876. [[CrossRef](#)]

18. Buttler, A.; Spliethoff, H. Current status of water electrolysis for energy storage, grid balancing and sector coupling via power-to-gas and power-to-liquids: A review. *Renew. Sustain. Energy Rev.* **2018**, *82*, 2440–2454. [[CrossRef](#)]
19. Wu, X.; Scott, K. A non-precious metal bifunctional oxygen electrode for alkaline anion exchange membrane cells. *J. Power Sources* **2012**, *206*, 14–19. [[CrossRef](#)]
20. Pavel, C.C.; Cecconi, F.; Emiliani, C.; Santuccioli, S.; Scaffidi, A.; Catanorchi, S.; Comotti, M. Highly efficient platinum group metal free based membrane-electrode assembly for anion exchange membrane water electrolysis. *Angew. Chem. Int. Ed.* **2014**, *53*, 1378–1381. [[CrossRef](#)]
21. Xiao, L.; Zhang, S.; Pan, J.; Yang, C.; He, M.; Zhuang, L.; Lu, J. First implementation of alkaline polymer electrolyte water electrolysis working only with pure water. *Energy Environ. Sci.* **2012**, *5*, 7869. [[CrossRef](#)]
22. Yang, Y.; Zhuang, L.; Rufford, T.E.; Wang, S.; Zhu, Z. Efficient water oxidation with amorphous transition metal boride catalysts synthesized by chemical reduction of metal nitrate salts at room temperature. *RSC Adv.* **2017**, *7*, 32923–32930. [[CrossRef](#)]
23. Nie, M.; Zou, Y.C.; Huang, Y.M.; Wang, J.Q. Ni-Fe-B catalysts for NaBH<sub>4</sub>hydrolysis. *Int. J. Hydrogen Energy* **2012**, *37*, 1568–1576. [[CrossRef](#)]
24. Mironova-Ulmane, N.; Kuzmin, A.; Steins, I.; Grabis, J.; Sildos, I.; Pärs, M. Raman scattering in nanosized nickel oxide NiO. *J. Phys. Conf. Ser.* **2007**, *93*. [[CrossRef](#)]
25. Wagner, C.D.; Riggs, W.M.; Davis, L.E.; Moulder, J.F.F.; Muilenberg, G.; Stickle, W.F.; Sobol, P.; EBomben, K.D. Handbook of X-Ray Photoelectron Spectroscopy. *Surf. Interface Anal.* **1979**, *3*, 80–90.
26. Sun, Y.; Hu, X.; Luo, W.; Huang, Y. Ultrafine MoO<sub>2</sub> nanoparticles embedded in a carbon matrix as a high-capacity and long-life anode for lithium-ion batteries. *J. Mater. Chem.* **2012**, *22*, 425–431. [[CrossRef](#)]
27. Kabir, S.A.; Lemire, K.; Artyushkova, K.; Roy, A.; Odgaard, M.; Schlueter, D.; Oshchepkov, A.; Bonnefont, A.; Savinova, E.; Sabarirajan, D.C.; et al. Platinum Group Metal-free NiMo Hydrogen Oxidation Catalysts: High Performance and Durability in Alkaline Exchange Membrane Fuel Cells. *J. Mater. Chem. A* **2017**, *5*, 24433–24443. [[CrossRef](#)]
28. Gupta, S.; Patel, N.; Fernandes, R.; Kadrekar, R.; Dashora, A.; Yadav, A.K.; Bhattacharyya, D.; Jha, S.N.; Miotello, A.; Kothari, D.C. Co-Ni-B nanocatalyst for efficient hydrogen evolution reaction in wide pH range. *Appl. Catal. B Environ.* **2016**, *192*, 126–133. [[CrossRef](#)]
29. Gupta, S.; Patel, N.; Fernandes, R.; Hanchate, S.; Miotello, A.; Kothari, D.C. Co-Mo-B Nanoparticles as a non-precious and efficient Bifunctional Electrocatalyst for Hydrogen and Oxygen Evolution. *Electrochim. Acta* **2017**, *232*, 64–71. [[CrossRef](#)]
30. McCrory, C.C.L.; Jung, S.; Peters, J.C.; Jaramillo, T.F. Benchmarking Heterogeneous Electrocatalysts for the Oxygen Evolution Reaction. *J. Am. Chem. Soc.* **2013**, *135*, 16977–16987. [[CrossRef](#)] [[PubMed](#)]
31. Voiry, D.; Chhowalla, M.; Gogotsi, Y.; Kotov, N.A.; Li, Y.; Penner, R.M.; Schaak, R.E.; Weiss, P.S. Best Practices for Reporting Electrocatalytic Performance of Nanomaterials. *ACS Nano* **2018**, *12*, 9635–9638. [[CrossRef](#)]
32. Rudi, S.; Cui, C.; Gan, L.; Strasser, P. Comparative Study of the Electrocatalytically Active Surface Areas (ECSAs) of Pt Alloy Nanoparticles Evaluated by Hupdand CO-stripping voltammetry. *Electrocatalysis* **2014**, *5*, 408–418. [[CrossRef](#)]
33. Deng, X.; Öztürk, S.; Weidenthaler, C.; Tüysüz, H. Iron-Induced Activation of Ordered Mesoporous Nickel Cobalt Oxide Electrocatalyst for the Oxygen Evolution Reaction. *ACS Appl. Mater. Interfaces* **2017**, *9*, 21225–21233. [[CrossRef](#)]
34. Shinagawa, T.; Garcia-Esparza, A.T.; Takanabe, K. Insight on Tafel slopes from a microkinetic analysis of aqueous electrocatalysis for energy conversion. *Sci. Rep.* **2015**, *5*, 1–21. [[CrossRef](#)] [[PubMed](#)]
35. Nickel Price. 2018. Available online: <https://markets.businessinsider.com/commodities/nickel-price> (accessed on 16 November 2018).
36. Mukherjee, A.; Chakrabarty, S.; Su, W.-N.; Basu, S. Nanostructured nickel ferrite embedded in reduced graphene oxide for electrocatalytic hydrogen evolution reaction. *Mater. Today Energy* **2018**, *8*, 118–124. [[CrossRef](#)]
37. Saha, S.; Ojha, K.; Sharma, M.; Ganguli, A.K. Ni<sub>3</sub>Co/G alloy as an earth-abundant robust and stable electrocatalyst for the hydrogen evolution reaction. *New J. Chem.* **2017**, *41*, 5916–5923. [[CrossRef](#)]
38. Franceschini, E.A.; Lacconi, G.I.; Corti, H.R. Kinetics of the hydrogen evolution on nickel in alkaline solution: New insight from rotating disk electrode and impedance spectroscopy analysis. *Electrochim. Acta* **2015**, *159*, 210–218. [[CrossRef](#)]

39. Dedigama, I.; Angeli, P.; Ayers, K.; Robinson, J.B.; Shearing, P.R.; Tsaoulidis, D.; Bret, D.J.L. In situ diagnostic techniques for characterisation of polymer electrolyte membrane water electrolyzers—Flow visualisation and electrochemical impedance spectroscopy. *Int. J. Hydrogen Energy* **2014**, *39*, 4468–4482. [[CrossRef](#)]
40. Kraglund, M.R.; Aili, D.; Jankova, K.; Christensen, E.; Li, Q.; Jensen, J.O. Zero-Gap Alkaline Water Electrolysis Using Ion-Solvating Polymer Electrolyte Membranes at Reduced KOH Concentrations. *J. Electrochem. Soc.* **2016**, *163*, F3125–F3131. [[CrossRef](#)]
41. Siracusano, S.; Trocino, S.; Briguglio, N.; Baglio, V.; Aricò, A.S. Electrochemical impedance spectroscopy as a diagnostic tool in polymer electrolyte membrane electrolysis. *Materials* **2018**, *11*, 1368. [[CrossRef](#)]
42. Fleig, J. The Influence of Current Constriction on the Impedance of Polarizable Electrodes. *J. Electrochem. Soc.* **1997**, *144*, L302. [[CrossRef](#)]
43. Newman, J.; Thomas, K.E. *Electrochemical Systems*, 3rd ed.; Wiley-Interscience: Hoboken, NJ, USA, 2004.
44. Sun, S.; Shao, Z.; Yu, H.; Li, G.; Yi, B. Investigations on degradation of the long-term proton exchange membrane water electrolysis stack. *J. Power Sources* **2014**, *267*, 515–520. [[CrossRef](#)]
45. Jaouen, F.; Lindbergh, G.; Wiezell, K. Transient Techniques for Investigating Mass-Transport Limitations in Gas Diffusion Electrodes. *J. Electrochem. Soc.* **2003**, *150*, A1711. [[CrossRef](#)]
46. Darab, M.; Barnett, A.O.; Lindbergh, G.; Thomassen, M.S.; Sunde, S. The Influence of Catalyst Layer Thickness on the Performance and Degradation of PEM Fuel Cell Cathodes with Constant Catalyst Loading. *Electrochim. Acta* **2017**, *232*, 505–516. [[CrossRef](#)]
47. Vincent, I.; Bessarabov, D. Low cost hydrogen production by anion exchange membrane electrolysis: A review. *Renew. Sustain. Energy Rev.* **2018**, *81*, 1690–1704. [[CrossRef](#)]
48. Fernandes, R.; Patel, N.; Miotello, A.; Filippi, M. Studies on catalytic behavior of Co-Ni-B in hydrogen production by hydrolysis of NaBH<sub>4</sub>. *J. Mol. Catal. A Chem.* **2009**, *298*, 1–6. [[CrossRef](#)]
49. Patel, N.; Fernandes, R.; Miotello, A. Promoting effect of transition metal-doped Co-B alloy catalysts for hydrogen production by hydrolysis of alkaline NaBH<sub>4</sub> solution. *J. Catal.* **2010**, *271*, 315–324. [[CrossRef](#)]



© 2018 by the authors. Licensee MDPI, Basel, Switzerland. This article is an open access article distributed under the terms and conditions of the Creative Commons Attribution (CC BY) license (<http://creativecommons.org/licenses/by/4.0/>).